

Structural, optical, and thermal properties of BN thin films grown on diamond via pulsed laser deposition

Abhijit Biswas^{1,*}, Gustavo A. Alvarez,² Tao Li³, Joyce Christiansen-Salameh,² Eugene Jeong², Anand B. Puthirath,¹ Sathvik Ajay Iyengar,¹ Chenxi Li,¹ Tia Gray,¹ Xiang Zhang,¹ Tymofii S. Pieshkov,^{1,4} Harikishan Kannan,¹ Jacob Elkins,¹ Robert Vajtai¹, A. Glen Birdwell,⁵ Mahesh R. Neupane,⁵ Elias J. Garratt,⁵ Bradford B. Pate,⁶ Tony G. Ivanov,⁵ Yuji Zhao,³ Zhiting Tian,^{2,†} and Pulickel M. Ajayan^{1,‡}

¹Department of Materials Science and Nanoengineering, Rice University, Houston, Texas 77005, USA


²Sibley School of Mechanical and Aerospace Engineering, Cornell University, Ithaca, New York 14853, USA

³Department of Electrical and Computer Engineering, Rice University, Houston, Texas 77005, USA

⁴Applied Physics Graduate Program, Smalley-Curl Institute, Rice University, Houston, Texas 77005, USA

⁵DEVCOM Army Research Laboratory, RF Devices and Circuits, Adelphi, Maryland 20783, USA

⁶Naval Research Laboratory, Chemistry Division, Washington, District of Columbia 20375, USA

 (Received 12 July 2023; revised 13 August 2023; accepted 30 August 2023; published 20 September 2023)

Heterostructures based on ultrawide-bandgap (UWBG) semiconductors (bandgap > 4.0 eV), such as BN and diamond, hold significant importance for the development of high-power electronics in the next generation. However, achieving *in situ* heteroepitaxy of BN/diamond or vice versa remains exceptionally challenging due to the complex growth kinetics involved. In this work, we grew BN thin film on (100) single-crystal diamonds using pulsed laser deposition and investigated its structural, magnetic, optical, and thermal properties. The structural analyses confirmed the growth of BN films, which exhibited diamagnetic behavior at room temperature. Notably, the film demonstrated anisotropic refractive index characteristics within the visible-to-near-infrared wavelength range. The room-temperature cross-plane thermal conductivity of BN is 1.53 ± 0.77 W/mK, while the thermal conductance of the BN/diamond interface is 20 ± 2 MW/m²K. These findings have significant implications for a range of device applications based on UWBG BN/diamond heterostructures.

DOI: [10.1103/PhysRevMaterials.7.094602](https://doi.org/10.1103/PhysRevMaterials.7.094602)

I. INTRODUCTION

Epitaxial integration of ultrawide-bandgap (UWBG) semiconductors (bandgap > 4.0 eV) represent a revolutionary new arena in materials research since they show excellent promise for high-performance electronics [1–4]. Typical existing UWBG semiconductors are diamond, BN, AlGaIn/AlN, and β -Ga₂O₃ [1–4]. Since the figure of merit of a device scales with the bandgap [1], these UWBG semiconductors show compelling advantages over their wide bandgap (WBG) counterparts (e.g., GaN and SiC), especially for high-power rf electronics, deep-UV optoelectronics, quantum information, thermal management, and for harsh environmental applications [5,6]. Despite their tremendous potential, however, the research on UWBG semiconductors is still premature, as integrating UWBG semiconductors with smooth and trapped-charges-free interfaces remains very challenging [1]. It is extremely important for the improved device performance with the reduced interfacial scattering to supersede the WBG technology [1].

According to the Baliga figure of merit, diamond and cubic BN (c-BN), the two strongest materials, show great potential in devices, with a high breakdown voltage ($\sim 10^4$ V

and a lower loss per switching cycle [1]. Diamond (bandgap $E_g \sim 5.5$ eV) and c-BN ($E_g \sim 6.2$ eV) are structurally, chemically, thermally, and electrically compatible [Fig. 1(a)] [7]. Electronically, both *p*- and *n*-type doping are possible in c-BN, while only *p*-type doping is achievable for diamond [1–3]. A high-mobility field-effect transistor (FET) is thus feasible by making heterojunctions of *n*-type c-BN and *p*-type diamond [1–3]. Therefore, extensive efforts are ongoing for the *in situ* fabrication of electronic quality UWBG c-BN/diamond thin-film heterostructures or vice versa [8–17].

In situ epitaxial thin-film growth of single-crystalline electronic quality pure or doped c-BN on structurally lattice-matched diamond and vice versa is the holy grail for UWBG devices. For BN polymorphs, the most stable phase is the two-dimensional (2D) hexagonal BN (h-BN) structure ($E_g \sim 5.9$ eV), whereas three-dimensional c-BN is the metastable phase and forms only at high temperature and pressure [Fig. 1(a)] [7,18]. Depending on the pressure and temperature during growth, BN forms various polymorphs and thus mixed-phase films [8–17]. Zhang *et al.* [8,12] wrote comprehensive reviews on the growth-related issues of mixed-phase BN film on silicon and diamond. Shtansky *et al.* [10] made efforts to provide the mechanism of mixed-phase BN growth on silicon. Narayan *et al.* [14] showed the direct conversion of h-BN into nano-ordered c-BN by nanosecond pulsed laser melting. Hiramra *et al.* [15,16] grew films with an abrupt interface on diamond and observed that a high temperature is important for c-BN growth. Therefore, as an alternative, *ex situ*

*01abhijit@gmail.com

†zhiting@cornell.edu

‡ajayan@rice.edu

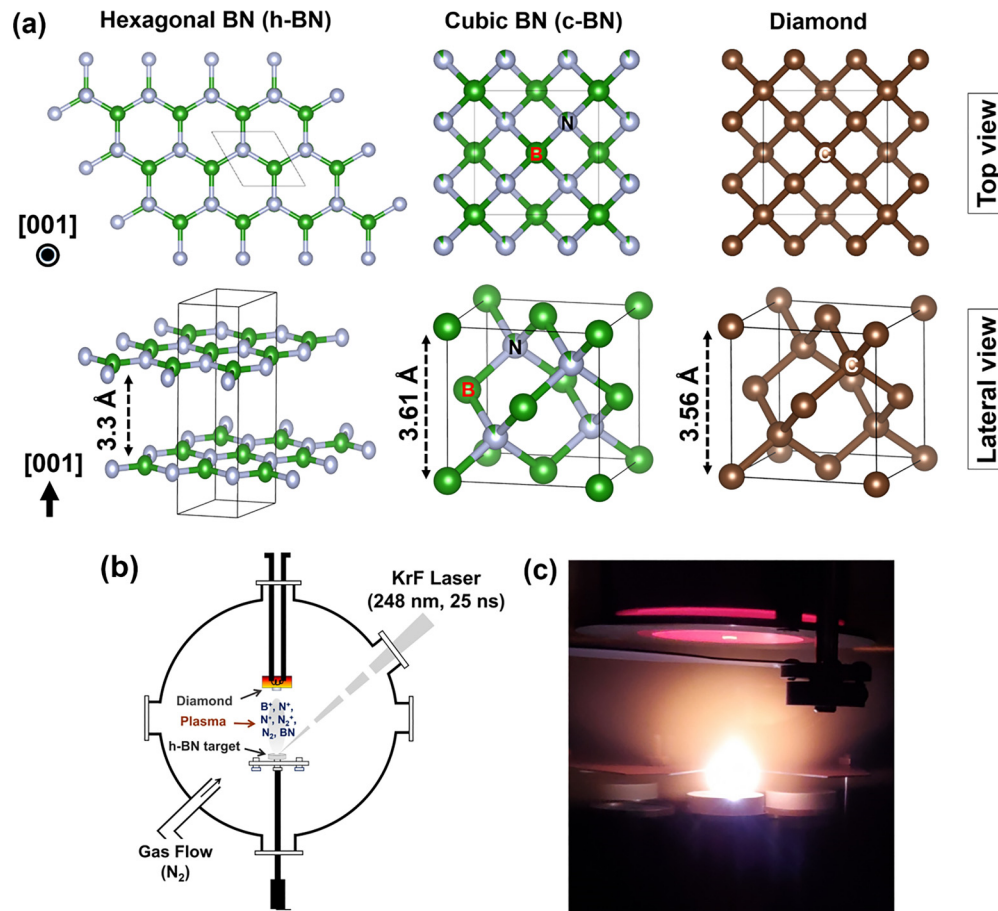


FIG. 1. (a) Structural compatibility of hexagonal and cubic boron nitride, and diamond (upper panel: top view; lower panel: lateral view). (b) Schematic of the pulsed laser deposition process. (c) Image captured during real-time growth showing laser-ablated plasma traveling toward the diamond substrate (kept on a hot substrate holder facing downward). Structures are drawn using VESTA software.

mechanically transferred h-BN flakes on single-crystal diamond (SCD) has been used as a gate dielectric in some diamond-based devices [19,20]. These diamond FETs show moderate mobility due to defects at the h-BN/SCD interface. Hence, there is a desperate need for the *in situ* growth of a defect-free thin layer of BN on a (100) SCD with a clean interface. Of greater significance, the measurement of relevant optical and thermal properties holds importance for the advancement of UWBG diamond-based high-power electronics.

In the literature, several efforts have been made to grow BN, especially c-BN films, by chemical vapor deposition (CVD) or molecular beam epitaxy [8–17]. However, it forms mixed-phase nanocrystalline BN, with interfacial defects (e.g., stacking faults) because of the complex growth kinetics. It has been predicted that additional energy is required to adatoms during growth [8,9]. Thus, the use of highly energetic, nonequilibrium pulsed laser deposition (PLD) might be an appropriate process. The advantages of PLD is the use of a dense target (single or polycrystalline) that is ablated by a highly energetic (2 to 5 eV) UV pulsed laser in the presence of partial gas pressure. PLD also offers faithful transfers of elements from the target-to-substrate surface in the form of plasma (in a stoichiometric ratio), endowed with the transfer of high-energy radicals and ions (B⁺, N^{*}, N₂^{*}, B⁺, N⁺, BN), with a kinetic energy of ~10 to 100 eV [Fig. 1(b) and 1(c)]

[21]. These ablated energetic species travel to the substrate within a few microseconds and coalesce to form a structure similar to the substrate, thus resulting in epitaxial film growth.

We grew BN thin film on (100) SCD substrates by PLD and performed structural, magnetic, optical, and thermal characterizations. Structural characterizations confirm the growth of BN. The films show diamagnetic behavior, have an anisotropic refractive index (RI) within the visible-to-near-infrared wavelength range, have an excellent cross-plane thermal conductivity (k_{\perp}) of 1.53 ± 0.77 W/mK, and an interfacial thermal conductance of 20 ± 2 MW/m²K at room temperature. These *in situ*-grown BN films on diamond by PLD, with the exhibition of various functionalities, might be useful for optoelectronic and critical thermal management applications.

II. RESULTS AND DISCUSSION

A. Diamond substrate characterizations

For depositions, we used commercially available normal-grade (100) SCD substrates (SKU 145-500-0549, size: 3×3 mm²) purchased from Element Six (United Kingdom). Since the surface of diamond is crucial [1,7], we first characterized the quality of the SCD. We performed x-ray diffraction (XRD) using the Rigaku SmartLab x-ray diffractometer,

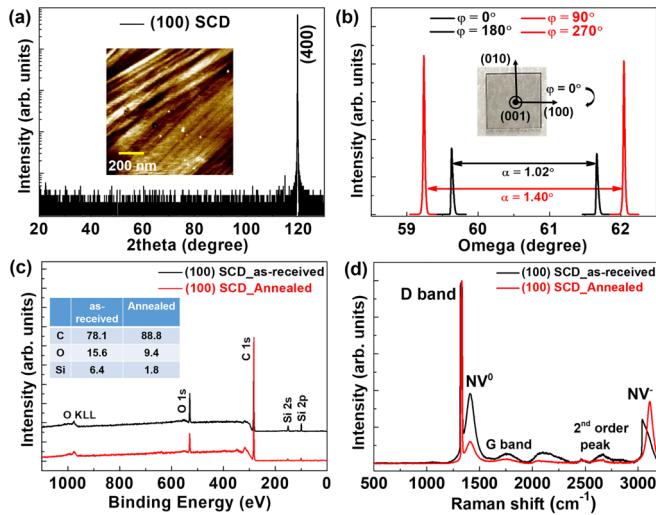


FIG. 2. (a) X-ray diffraction shows only the (400) peak. Inset: The atomic force microscopy image with a surface roughness of ~ 1.5 nm. (b) Rocking curve at four different azimuthal angles showing the average miscut angle of $\sim 1.2^\circ$. Inset: A diamond substrate ($\sim 3 \times 3$ mm²). (c) X-ray photoelectron spectroscopy of as-received and *in situ* annealed diamond surface, showing that the *in situ* annealed substrate has a lower concentration of silicon and oxygen. (d) Raman spectra show the characteristic *D*-band peak (~ 1333 cm⁻¹) corresponding to the vibration of the sp^3 diamond, along with the higher orders and nitrogen vacancy-related modes.

equipped with a monochromatic copper $K\alpha$ radiation source. Thin-film XRD show the presence of only a (400) peak throughout the θ - 2θ scan range, with a full width at half maximum (FWHM) of $\sim 0.03^\circ$ [Fig. 2(a)]. We obtained the miscut angle of the SCD by measuring the FWHM of (400) rocking curves at four different azimuthal angles, which was found to be $\sim 1.21^\circ$ [Fig. 2(b)]. The surface topography by atomic force microscopy shows a flat surface with a surface roughness of ~ 1.5 nm [Fig. 2(a), inset]. X-ray photoelectron spectroscopy (XPS) (performed using the PHI Quantera SXM scanning x-ray microprobe with a 1486.6-eV monochromatic aluminum $K\alpha$ x-ray source and at a 26-eV pass energy) of the as-received SCD shows a carbon peak along with the presence of oxygen, and a silicon impurity [Fig. 2(c)]. Therefore, we annealed the SCD substrate at $\sim 750^\circ\text{C}$ and in a nitrogen partial pressure atmosphere ($P_{\text{N}_2} \sim 100$ mTorr) for an hour (inside the PLD chamber), which resulted in a notable reduction in both the oxygen and silicon concentrations. Raman spectra (using the Renishaw inVia confocal microscope with the 532-nm laser as the excitation source) show a strong *D*-band (~ 1333 cm⁻¹), along with the nitrogen vacancy-related peaks (NV⁰ and NV⁻), *G*-band, and second-order Raman spectrum [Fig. 2(d)] [22]. These vacancy-related peaks are reduced after high-temperature *in situ* annealing. Therefore, it is a necessity to perform *in situ* annealing of SCD substrates before thin-film deposition.

B. Thin-film growth and structural characterizations

BN thin films ~ 20 -nm thick were grown using PLD [load lock-assisted high-vacuum ($\sim 5 \times 10^{-9}$ Torr) chamber oper-

ating with a KrF excimer laser (with a 248-nm wavelength and a pulse width of 25 ns)]. The films were grown using the following conditions: growth temperature, $\sim 750^\circ\text{C}$; P_{N_2} , ~ 100 mTorr; laser fluency, ~ 2.2 J/cm²; target-to-substrate distance, ~ 50 mm; and repetition rate, 5 Hz. For the ablation, we used a commercially available 1-in.-diameter h-BN target (American Element, 99.9%). Before and after each deposition, the SCD and BN/SCD were pre- and postannealed at the same growth temperature and pressure for 1 h. For the depositions, 2000 laser pulses were supplied. After growth, films were cooled at $\sim 20^\circ\text{C}/\text{min}$.

We performed core-level XPS, which shows the presence of characteristic B-N bonding peaks at ~ 190.4 eV (boron 1s core) and at ~ 397.9 eV (nitrogen 1s core) [Fig. 3(a) and (b)] [23,24]. Using XPS, we also observed the plasmon's peaks (at ~ 9 eV and ~ 25 eV apart from the main B-N peak), which is characteristic of h-BN [25]. The XPS valence band spectra (XPS-VBS) was acquired using a pass energy of 69 eV. The XPS-VBS show that the valence band maxima is ~ 1.8 eV below the Fermi level [Fig. 3(c)]. The films show a smooth surface with a roughness of ~ 2.88 nm [Fig. 3(d)]. In the Raman spectra, we observed a peak at ~ 1053 cm⁻¹, which corresponds to the c-BN transverse optical (TO) phonon mode [Fig. 3(e)] [8]. Moreover, intense and broad peaks within ~ 1350 to 1450 cm⁻¹ indicate the presence of an E_{2g} phonon mode of h-BN (along with an NV⁰ peak of the SCD). Furthermore, Fourier transform infrared (FTIR) spectra obtained with the Nicolet 380 FTIR spectrometer using a single-crystal germanium window shows the TO phonon modes (both in-plane and out-of-plane modes of c-BN and h-BN) [Fig. 3(f)] [8,24].

To get more insights about the crystallinity and phase of BN, cross-sectional high-resolution transmission electron microscopy was conducted [Fig. 4(a)]. The obtained cross-sectional image clearly shows the presence of BN, which is further supported by electron energy loss spectroscopy (EELS) elemental mapping [Fig. 4(b)]. Corresponding boron and nitrogen *K*-edges from the EEL spectra are also presented [Fig. 4(c)]. The EELS spectra closely resemble the literature reports [26,27], indicating the presence of different phases of BN. The boron spectrum displays a distinct and narrow π^* peak, reminiscent of h-BN. Additionally, a broader and slightly weaker σ^* peak is also observed. The presence of both peaks suggests the coexistence of sp^2 -bonded h-BN and a sp^3 -bonded BN, which is probably the nucleation sites for c-BN [27]. The nitrogen spectrum also resembles the feature of amorphous BN (a-BN) or c-BN, with a marginally intense π^* peak than the broader and intense σ^* peak [26,27]. Furthermore, comparing the $sp^2 : sp^3$ ratio in the boron spectrum, it is evident that the volume fraction of sp^2 is slightly higher than the sp^3 BN (seen in the FTIR as well [Fig. 3(f)]) [26].

Considering the structural and chemical compatibility, c-BN is more favorable to grow on a SCD, and thus extensive efforts are ongoing to understand the complex mixed-phase growth of BN on a SCD [8–10]. At ambient conditions, h-BN is the most thermodynamically stable phase. However, several theoretical predictions suggest that c-BN is stable at ambient conditions [28,29], making the growth kinetics complicated for pure c-BN phase film optimization. The huge

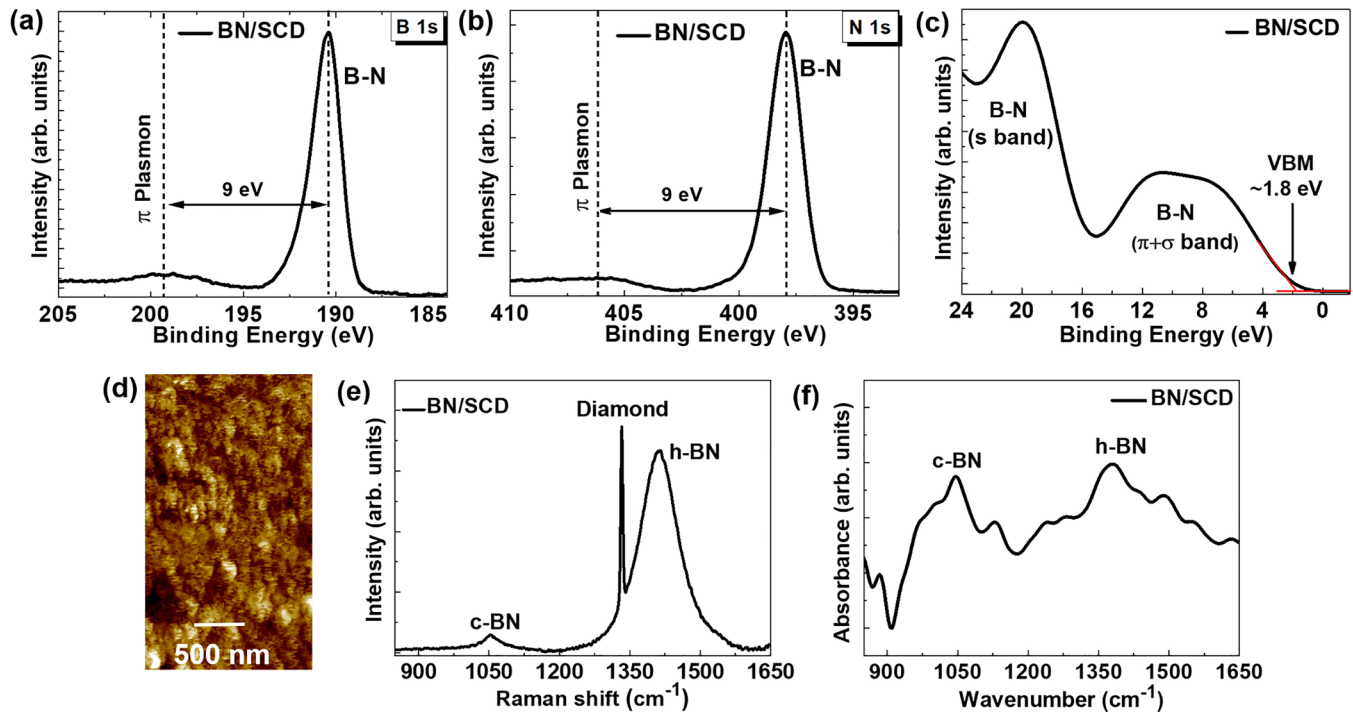


FIG. 3. (a) and (b) X-ray photoelectron spectroscopy shows the characteristic B-N bonding with plasmon peaks. (c) The XPS-VBS, with characteristics *s*-band and π - + σ -band. (d) Atomic force microscopy of BN surface. (e) and (f) Raman and FTIR spectra of film.

kinetic barrier hinders the transformation of sp^2 - h-BN (ionic) to sp^3 -bonded (covalent) c-BN [30]. Therefore, it is thought that c-BN growth could be achieved by providing additional energy during growth (e.g., high-temperature growth kinetics, using ion beam-assisted growth, and postgrowth thermal treatment) [8–10,31,32]. However, these approaches develop additional stress, producing nanocrystalline films with defective interfaces [33–35]. Recently, magnesium was used

as a catalyst to reduce the energy barrier and promote c-BN growth; however, films remained in the nanocrystalline phase [36]. We carried out growth at high temperatures and followed it with thermal annealing. Our method also resulted in the formation of BN, although it is likely to have a combination of different phases. Existing literature shows that noncrystalline amorphous semiconductors (absence of a long-range crystalline nature) possess exceptional functional properties, making them highly valuable in the field of electronics [37,38].

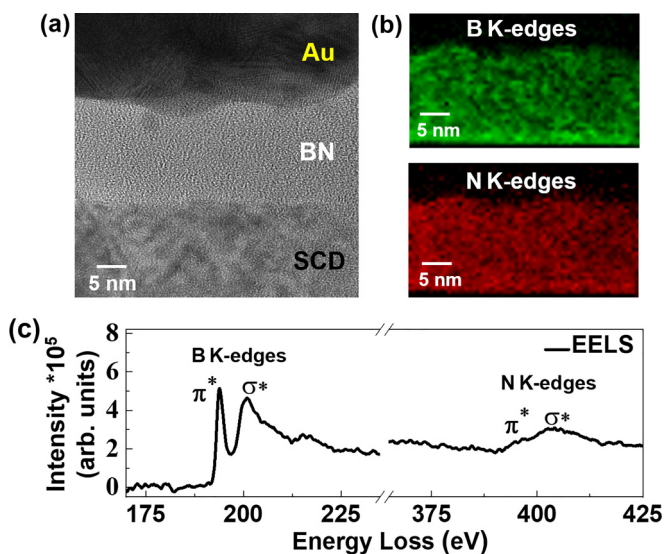


FIG. 4. (a) Cross-sectional high-resolution transmission electron microscopic image of BN film on a SCD. (b) EELS elemental mapping shows the presence of both boron and nitrogen. (c) EELS showing the bands corresponding to boron and nitrogen *K*-edges.

C. Magnetic, optical, and thermal characterization of films

The magnetic properties of BN are also interesting [39]. Neither boron nor nitrogen has any unpaired electrons, thus the single-crystal, defect-free BN does not exhibit any magnetic response. However, the incorporation of dopants (e.g., carbon or fluorine) or vacancies results in a ferromagnetic response (formation of local moments) above room temperature [39]. Thus, it is worthwhile to explore the magnetic properties of BN films. We investigated the room-temperature magnetic hysteresis loop of the film. Room-temperature magnetic hysteresis (moment vs. magnetic field) measurements were acquired using a SQUID-VSM-7 Tesla (Quantum Design, USA) within a magnetic field sweep range of ± 5 Tesla. The film remains diamagnetic throughout the magnetic field scanning range [Fig. 5(a)], indicating that the grown BN film is free of defects or vacancies (also supports the XPS elemental scans showing a B:N ratio of $\sim 1 : 1$; precisely, 35.4:35.2) within the detection limit of the SQUID instrument.

We measured the optical refractive index of the film (wavelength range, 300 to 1600 nm). A variable-angle spectroscopic ellipsometer (M-2000 Ellipsometer) was used to measure the

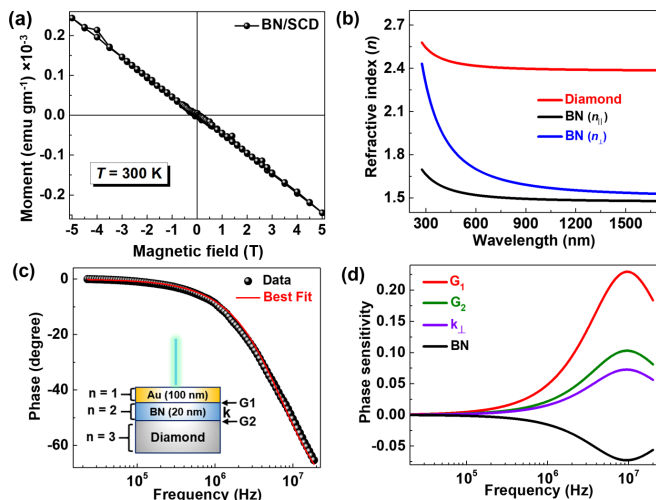


FIG. 5. (a) Room-temperature magnetic hysteresis loop shows the diamagnetic behavior. (b) In-plane and out-of-plane refractive index of BN film and diamond within the visible-to-near-infrared wavelength. (c) Phase-versus-frequency data for BN. Inset: The multilayer sample model where each layer includes the volumetric heat capacity (c_p), k_{\perp} and k_{\parallel} , layer thickness, and G_1 and G_2 . (d) Sensitivity analysis of G_1 between gold and BN, k_{\perp} of BN, and G_2 between the BN and diamond.

RI of a pristine SCD (as a reference), followed by the RI of BN. The process involves illuminating the samples with light at four equally spaced incident angles (Φ) ranging from 55° to 70° and collecting the reflected light to get the reflection coefficients for both s -polarized and p -polarized lights of the samples, fitted to obtain the RI. For fitting, we constructed a two-layer model to represent the BN/SCD heterostructure, with an anisotropic uniaxial Cauchy model applied to the top layer [38]. This approach resulted in a mean square error of ~ 13.6 and a physical normal dispersion across the entire wavelength region. For BN film, we obtained a RI of ~ 1.5 to 1.7 (in plane, n_{\parallel}) and ~ 1.6 to 2.4 (out of plane, n_{\perp}) [Fig. 5(b)]. In the literature, the RI is ~ 1.9 (h-BN, in plane), ~ 1.5 (h-BN, out of plane), and ~ 2.2 (c-BN) in the visible-to-near-infrared wavelength range [40,41]. Note, for a-BN the RI is much lower (~ 1.37 at 633 nm) [38]. Also, for h-BN, ideally the out-of-plane RI should be lower than the in-plane RI due to its 2D nature [40]. However, we observed the opposite trend (i.e., $n_{\parallel} < n_{\perp}$) [40]. This could be useful for the precise design of UWBG-based optoelectronic (especially photonic) devices [42].

Moreover, interfacial thermal transport between the UWBG semiconductors plays an important role in thermal management applications while fabricating electronic devices. Therefore, we measured the thermal boundary conductance (G) and k_{\perp} using the optical pump-probe method, frequency domain thermoreflectance (FDTR). An electro-optic modulator induced a sinusoidal intensity modulation on a 488-nm pump continuous-wave laser, creating a periodic heat flux on the sample surface [43]. An unmodulated 532-nm continuous-wave probe laser monitored the surface temperature through a change in surface reflectivity. We compared the calculated phase lag of the sample surface temperature, in-

duced by a periodic heat source at the sample surface, against the measured phase lag of the balanced probe beam (measured with respect to the reference signal from the lock-in amplifier) [44].

The sample is modeled as a three-layer system, where each layer includes the volumetric heat capacity c_p , k_{\perp} and in-plane thermal conductivity (k_{\parallel}), layer thickness, and thermal boundary conductance G_1 and G_2 [Fig. 5(c), inset]. Gold was chosen as a transducer layer to maximize the coefficient of thermoreflectance at the probe wavelength. The measurement of individual material physical properties was performed as an inverse problem, minimizing the error between the calculated phase and the measured lock-in phase data via a nonlinear least-squares algorithm [41]. A more comprehensive description of solving this equation is detailed by Schmidt *et al.* [44]. An example of the phase-versus-frequency data obtained from FDTR with an average of three runs acquired on one spot location is provided [Fig. 5(c)]. The data are in good approximation to the best-fit curve obtained from solving the heat diffusion equation. Furthermore, a sensitivity analysis was also conducted to determine which parameters could be fit together. The k_{\perp} of BN is the parameter of interest and it is most sensitive at higher frequencies [Fig. 5(d)]. The G_1 between gold and BN, G_2 between BN and diamond, and the thickness of BN are also most sensitive at higher frequencies. Thus, the focus is primarily on fitting the k_{\perp} of BN and G_2 . From the average of three runs on three separate spot locations on the sample (i.e., a total of nine measurements), we determined a k_{\perp} for BN of 1.53 ± 0.77 W/mK and a thermal conductance of the BN/SCD interface of $G_2 = 20 \pm 2$ MW/m²K. These values are slightly lower than those for bulk single-crystalline h-BN (4.8 W/mK and 60 MW/m²K) [45]. Brown *et al.* [46] obtained a thermal boundary conductance of 33.7 MW/m²K for h-BN grown on copper foil by CVD. Glavin *et al.* [47] obtained a much lower thermal conductance of a-BN (between 1 and 5 MW/m²K) grown by PLD by using different metal contacts. Considering the next generation of high-power electronics, information on the thermal conductivity and interfacial thermal boundary conductance of BN/diamond is of paramount importance due to their critical role in heat dissipation, thermal management, high-temperature operation, power density handling, and overall device reliability. These factors collectively contribute to the efficient and reliable operation of UWBG devices across a wide range of applications.

III. CONCLUSION

To summarize, BN thin films were successfully grown on (100) diamond single crystals using PLD. Detailed structural analyses have confirmed the growth of these thin films. We investigated several properties through measurements of the optical refractive index, magnetization, and thermal conductivity. While these properties are appealing, further endeavors are required to grow BN/diamond heterostructures with high-quality electronic interfaces in the future. Nonetheless, given the pressing demand for *in situ* integrations with clean interfaces in high-power UWBG semiconductor electronics, our demonstration holds potential for fabricating BN/diamond devices suitable for diverse applications.

The data of this study are available from the corresponding author upon reasonable request.

ACKNOWLEDGMENTS

This work was sponsored partly by the Army Research Office and was accomplished under Cooperative Agreement No. W911NF-19-2-0269. This work was also partly supported as part of ULTRA, an Energy Frontier Research Center funded by the U.S. Department of Energy, Office of Science, Basic Energy Sciences (Award No. DE-SC0021230), and in part by CHIMES, one of the seven centers in JUMP 2.0, a Semiconductor Research Corporation (SRC) program sponsored by DARPA. This work was also partly sponsored by the Department of the Navy, Office of Naval Research (ONR Award No. N00014-22-1-2357), and by the National Science Foundation Graduate Research Fellowship (Grant No. 1650114). This work was performed, in part, at the Cornell NanoScale

Facility, a member of the National Nanotechnology Coordinated Infrastructure (NNCI), which is supported by the National Science Foundation (Grant No. NNCI-2025233). This work made use of the Cornell Center for Materials Research Shared Facilities, which are supported through the NSF MRSEC program (Grant No. DMR-1719875). A.B. thanks Dr. Jianhua Li for kind help. The views and opinions of authors expressed herein do not necessarily state or reflect those of the United States Government or any agency thereof.

A.B., R.V., and P.M.A. conceptualized the study. A.B., C.L., S.A.I., X.Z., H.K., T.G. and J.L. grew and characterized the films. A.B.P. and T.P. performed the focused ion beam (FIB) and electron microscopy. T.L. and Y.Z. carried out the optical measurement. G.A., J.C., E.J., and Z.T. measured thermal conductivity. A.G.B., M.R.N., E.G., B.B.P., and T.I. commented on the manuscript. All authors discussed the results and contributed on the manuscript preparation.

-
- [1] J. Y. Tsao *et al.*, Ultrawide-bandgap semiconductors: Research opportunities and challenges, *Adv. Electron. Mater.* **4**, 1600501 (2018).
- [2] S. J. Bader, H. Lee, R. Chaudhuri, S. Huang, A. Hickman, A. Molnar, H. G. Xing, D. Jena, H. W. Then, N. Chowdhury, and T. Palacios, Prospects for wide bandgap and ultrawide bandgap CMOS devices, *IEEE Trans. Electron Devices.* **67**, 4010 (2020).
- [3] M. Higashiwaki, R. Kaplar, J. Pernot, and H. Zhao, Ultrawide bandgap semiconductors, *Appl. Phys. Lett.* **118**, 200401 (2021).
- [4] G. Alvarez-Escalante, R. Page, R. Hu, H. G. Xing, D. Jena, and Z. Tian, High thermal conductivity and ultrahigh thermal boundary conductance of homoepitaxial AlN thin films, *APL Mater.* **10**, 011115 (2022).
- [5] J. Ballestín-Fuertes, J. Muñoz-Cruzado-Alba, J. F. Sanz-Osorio, and E. Laporta-Puyal, Role of wide bandgap materials in power electronics for smart grids applications, *Electronics* **10**, 677 (2021).
- [6] M. Meneghini, C. D. Santi, I. Abid, M. Buffolo, M. Cioni, R. A. Khadar, L. Nela, N. Zagni, A. Chini, F. Medjdoub, G. Meneghesso, G. Verzellesi, E. Zanoni, and E. Matioli, GaN-based power devices: Physics, reliability, and perspectives, *J. Appl. Phys.* **130**, 181101 (2021).
- [7] S. N. Monteiro, A. L. D. Skury, M. G. de Azevedo, and G. S. Bobrovnichii, Cubic boron nitride competing with diamond as a superhard engineering material: An overview, *J. Mater. Res. Technol.* **2**, 68 (2013).
- [8] W. J. Zhang, Y. M. Chong, I. Bello, and S. T. Lee, Nucleation, growth and characterization of cubic boron nitride (cBN) films, *J. Phys. D Appl. Phys.* **40**, 6159 (2007).
- [9] W. Kulisch, R. Freudenstein, A. Klett, and M. F. Plass, A concept for the deposition of adherent cubic boron nitride films, *Thin Solid Films* **377-378**, 170 (2000).
- [10] D. V. Shtansky, Y. Yamada-Takamura, T. Yoshida, and Y. Ikuhara, Mechanism of nucleation and growth of cubic boron nitride thin films, *Sci. Technol. Adv. Mater.* **1**, 219 (2000).
- [11] V. Z. Turkevich, Phase diagrams and synthesis of cubic boron nitride, *J. Phys.: Condens. Matter* **14**, 10963 (2002).
- [12] W. J. Zhang, X. M. Meng, C. Y. Chan, K. M. Chan, Y. Wu, I. Bello, and S. T. Lee, Interfacial study of cubic boron nitride films deposited on diamond, *J. Phys. Chem. B* **109**, 16005 (2005).
- [13] C. B. Samantaray and R. N. Singh, Review of synthesis and properties of cubic boron nitride (c-BN) thin films, *Int. Mater. Rev.* **50**, 313 (2005).
- [14] J. Narayan, A. Bhaumik, and W. Xu, Direct conversion of h-BN into c-BN and formation of epitaxial c-BN/diamond heterostructures, *J. Appl. Phys.* **119**, 185302 (2016).
- [15] K. Hirama, Y. Taniyasu, S. Karimoto, H. Yamamoto, and K. Kumakura, Heteroepitaxial growth of single-domain cubic boron nitride films by ion-beam-assisted MBE, *Appl. Phys. Exp.* **10**, 035501 (2017).
- [16] K. Hirama, Y. Taniyasu, H. Yamamoto, and K. Kumakura, Structural analysis of cubic boron nitride (111) films heteroepitaxially grown on diamond (111) substrates, *J. Appl. Phys.* **125**, 115303 (2019).
- [17] X. W. Zhang, H.- G. Boyen, N. Deyneka, P. Ziemann, F. Banhart, and M. Schreck, Epitaxy of cubic boron nitride on (001)-oriented diamond, *Nat. Mater.* **2**, 312 (2003).
- [18] G. R. Bhimanapati, N. R. Glavin, and J. A. Robinson, 2D Boron nitride: Synthesis and applications, *Semicond. Semimet.* **95**, 101 (2016).
- [19] Y. Sasama, K. Komatsu, S. Moriyama, M. Imura, T. Teraji, K. Watanabe, T. Taniguchi, T. Uchihashi, and Y. Takahide, High-mobility diamond field effect transistor with a monocrystalline h-BN gate dielectric, *APL Mater.* **6**, 111105 (2018).
- [20] Y. Sasama, T. Kageura, M. Imura, K. Watanabe, T. Taniguchi, T. Uchihashi, and Y. Takahide, High-mobility p-channel wide-bandgap transistors based on hydrogen-terminated diamond/hexagonal boron nitride heterostructures, *Nat. Electron.* **5**, 37 (2022).
- [21] N. R. Glavin, C. Muratore, M. L. Jespersen, J. Hu, T. S. Fisher, and A. A. Voevodin, Temporally and spatially resolved plasma spectroscopy in pulsed laser deposition of ultra-thin boron nitride films, *J. Appl. Phys.* **117**, 165305 (2015).

- [22] V. S. Gorelik and A. Yu. Pyatyshev, Raman scattering in diamond nano- and microcrystals, synthesized at high temperatures and high pressures, *Diam. Relat. Mater.* **110**, 108104 (2020).
- [23] R. Y. Tay, S. H. Tsang, M. Loeblein, W. L. Chow, G. C. Loh, J. W. Toh, S. L. Ang, and E. H. T. Teo, Direct growth of nanocrystalline hexagonal boron nitride films on dielectric substrates, *Appl. Phys. Lett.* **106**, 101901 (2015).
- [24] S. Saha, A. Rice, A. Ghosh, S. M. N. Hasan, W. You, T. Ma, A. Hunter, L. J. Bissell, R. Bedford, M. Crawford, and S. Arafin, Comprehensive characterization and analysis of hexagonal boron nitride on sapphire, *AIP Adv.* **11**, 055008 (2021).
- [25] C. Zhi, S. Ueda, H. Zeng, X. Wang, W. Tian, X. Wang, Y. Bando, and D. Golberg, Weak morphology dependent valence band structure of boron nitride, *J. Appl. Phys.* **114**, 054306 (2013).
- [26] M. Lv, B. Xu, X. Gou, L. Cai, and X. Yuan, Electron energy loss spectroscopy analysis for cubic boron nitride single crystals transition mechanism in $\text{Li}_3\text{N-BN}$ system, *Mater. Lett.* **242**, 75 (2019).
- [27] J. Y. Huang, H. Yasuda, and H. Mori, HRTEM and EELS studies on the amorphization of hexagonal boron nitride induced by ball milling, *J. Am. Ceram. Soc.* **83**, 403 (2004).
- [28] V. L. Solozhenko, V. Z. Turkevich, and W. B. Holzapfel, Refined phase diagram of boron nitride, *J. Phys. Chem. B* **103**, 2903 (1999).
- [29] C. Cazorla and T. Gould, Polymorphism of bulk boron nitride, *Sci. Adv.* **5**, eaau5832 (2019).
- [30] P. B. Mirkarimi, K. F. McCarty, and D. L. Medlin, Review of advances in cubic boron nitride film synthesis, *Mater. Sci. Eng. R Rep.* **21**, 47 (1997).
- [31] H. Xin, Y. Chen, X. Shi, H. Xu, C. Lin, and S. Zou, Growth of cubic boron nitride thin films by a field-ionization source-assisted pulsed laser deposition, *Thin Solid Films* **266**, 173 (1995).
- [32] T. A. Friedmann, P. B. Mirkarimi, D. L. Medlin, K. F. McCarty, E. J. Klaus, D. R. Boehme, H. A. Johnsen, M. J. Mills, D. K. Ottesen, and J. C. Barbour, Ion-assisted pulsed laser deposition of cubic boron nitride films, *J. Appl. Phys.* **76**, 3088 (1994).
- [33] I.-H. Kim, K.-S. Kim, S.-H. Kim, and S.-R. Lee, Synthesis of cubic boron nitride films using a helicon wave plasma and reduction of compressive stress, *Thin Solid Films* **290-291**, 120 (1996).
- [34] P. B. Mirkarimi, D. L. Medlin, K. F. McCarty, D. C. Dibble, W. M. Clift, J. A. Knapp, and J. C. Barbour, The synthesis, characterization, and mechanical properties of thick, ultrahard cubic boron nitride films deposited by ion-assisted sputtering, *J. Appl. Phys.* **82**, 1617 (1997).
- [35] W. J. Yu, W. M. Lau, S. P. Chan, Z. F. Liu, and Q. Q. Zheng, *Ab initio* study of phase transformations in boron nitride, *Phys. Rev. B* **67**, 014108 (2003).
- [36] D. F. Storm, S. I. Maximenko, A. C. Lang, N. J. Nepal, T. I. Feygelson, B. B. Pate, C. A. Affouda, and D. J. Meyer, Mg-facilitated growth of cubic boron nitride by ion beam-assisted molecular beam epitaxy, *Phys. Status Solidi(RRL)* **16**, 2200036 (2022).
- [37] M. H. Cohen, Review of the theory of amorphous semiconductors, *J. Non-Cryst. Solids* **4**, 391 (1970).
- [38] S. Hong *et al.*, Ultralow-dielectric-constant amorphous boron nitride, *Nature (London)* **582**, 511 (2020).
- [39] C. Zhao, Z. Xu, H. Wang, J. Wei, W. Wang, X. Bai, and E. Wang, Carbon-doped boron nitride nanosheets with ferromagnetism above room temperature, *Adv. Mater.* **24**, 5985 (2014).
- [40] E. Franke, M. Schubert, J.-D. Hecht, H. Neumann, T. E. Tiwald, D. W. Thompson, H. Yao, J. A. Woollam, and J. Hahn, In situ infrared and visible-light ellipsometric investigations of boron nitride thin films at elevated temperatures, *J. Appl. Phys.* **84**, 526 (1998).
- [41] E. Franke, M. Schubert, H. Neumann, T. E. Tiwald, D. W. Thompson, J. A. Woollam, J. Hahn, and F. Richter, Phase and microstructure investigations of boron nitride thin films by spectroscopic ellipsometry in the visible and infrared spectral range, *J. Appl. Phys.* **82**, 2906 (1997).
- [42] J. D. Caldwell, I. Aharonovich, G. Cassaboris, J. H. Edgar, B. Gil, and D. N. Nasov, Photonics with hexagonal boron nitride, *Nat. Rev. Mater.* **4**, 552 (2019).
- [43] K. T. Regner, S. Majumdar, and J. A. Malen, Instrumentation of broadband frequency domain thermoreflectance for measuring thermal conductivity accumulation functions, *Rev. Sci. Instrum.* **84**, 064901 (2013).
- [44] A. J. Schmidt, R. Cheaito, and M. Chiesa, A frequency-domain thermoreflectance method for the characterization of thermal properties, *Rev. Sci. Instrum.* **80**, 94901 (2009).
- [45] P. Jiang, X. Qian, R. Yang, and L. Lindsay, Anisotropic thermal transport in bulk hexagonal boron nitride, *Phys. Rev. Mater.* **2**, 064005 (2018).
- [46] D. B. Brown, T. L. Bougher, X. Zhang, P. M. Ajayan, B. A. Cola, and S. Kumar, Thermal boundary conductance and phonon transmission in hexagonal boron nitride/graphene heterostructures, *Phys. Status Solidi (A) Appl. Mater. Sci.* **216**, 1900446 (2019).
- [47] N. R. Glavin, A. R. Waite, C. Muratore, J. E. Bultman, J. Hu, J. J. Gengler, A. A. Voevodin, and T. S. Fisher, Thermal conductance at nanoscale amorphous boron nitride/metal interfaces, *Surf. Coat. Technol.* **397**, 126017 (2020).